

Particle Shape Effects on Subvisible Particle Sizing Measurements

RICHARD E. CAVICCHI,¹ MICHAEL J. CARRIER,¹ JOSHUA B. COHEN,¹ SHIR BOGER,¹ CHRISTOPHER B. MONTGOMERY,¹ ZHISHANG HU,² DEAN C. RIPPLE¹

¹Bioprocess Measurements Group, National Institute of Standards and Technology, Gaithersburg, Maryland

²Center for Computational and Systems Biology, Institute of Biophysics Chinese Academy of Sciences, Beijing, China

Received 12 May 2014; revised 2 October 2014; accepted 21 October 2014

Published online 1 December 2014 in Wiley Online Library (wileyonlinelibrary.com). DOI 10.1002/jps.24263

ABSTRACT: Particle analysis tools for the subvisible (<100 μm) size range, such as light obscuration, flow imaging (FI), and electrical sensing zone (ESZ), often produce results that do not agree with one another, despite their general agreement when characterizing polystyrene latex spheres of different sizes. To include the effect of shape in comparison studies, we have used the methods of photolithography to create rods and disks. Although the rods are highly monodisperse, the instruments produce broadened peaks and report mean size parameters that are different for different instruments. We have fabricated a microfluidic device that simultaneously performs ESZ and FI measurements on each particle to elucidate the causes of discrepancies and broadening. Alignment of the rods with flow causes an oversizing by FI and undersizing by ESZ. FI also oversizes rods because of the incorrect edge definition that results from diffraction and imperfect focus. We present an improved correction algorithm for this effect that reduces discrepancies for rod-shaped particles. Tumbling of particles is observed in the microfluidic ESZ/FI and results in particle oversizing and breadth of size distribution for the monodisperse rods. © 2014 Wiley Periodicals, Inc. and the American Pharmacists Association *J Pharm Sci* 104:971–987, 2015

Keywords: electrical sensing zone; flow imaging; image analysis; light obscuration; light scattering (static); microscopy; particle sizing; physical characterization

INTRODUCTION

Sizing and counting of subvisible particles in therapeutic protein formulations is an increasingly important measurement task. The possibility of enhanced immune response ascribed to protein aggregates has been reviewed,¹ potentially leading to reduced efficacy or safety risks. A number of techniques for characterizing particle size and quantity are being investigated for this problem, including light obscuration (LO), flow imaging (FI), and electrical sensing zone (ESZ). Frequently these techniques report results that are in disagreement with one another^{2–4} unless the source of bias is identified and corrected for.

Data from these instruments are commonly presented in the form of histograms of number of particles versus a size dimension of the particle, typically reported as an equivalent spherical diameter (ESD) or equivalent circular diameter (ECD). The ESD is the diameter of a sphere that would produce a similar signal on the same instrument. An analogous definition applies for the ECD. Demeule et al.² compared the total particle count from an aged humanized IgG1 antibody for particles greater than a given size using LO, FI, and ESZ. They found that when the given size is 10 μm , the techniques gave similar results, whereas when the size is 2.75 μm , the three techniques gave counts that varied in the order from least to greatest: LO < FI < ESZ. It was suggested that the low optical contrast of the particles was responsible for the results. This was investigated further by Zolls et al.,⁵ who varied the index of refraction of the solution containing protein particles. It was found that formulations with increased index of refraction led to an underestimation of the particle count when measured using LO

or FI. The recommendation was to consider using orthogonal test methods that do not require optical contrast. These effects were confirmed in studies by Werk et al.⁴ where particles including polystyrene and glass beads as well as a new pseudo-protein particle standard were used in formulations of different color, viscosity, density, and refractive index. Translucent particles produced undersizing and lower counts, especially in LO measurements. For simple geometries, mathematical relations between different diameter definitions has been given by Jennings and Parslow.⁶

The ESZ method, or “Coulter Principle,” is a size measurement technique that records the resistance change when a particle in a conductive liquid transits a small orifice that separates two chambers. For protein analysis, the technique has the advantages of being unaffected by particle transparency, linear over a wide range of concentration, and operative over a wide size range (0.4 μm to >100 μm , although in a given measurement with fixed orifice the range covers a factor of 30).

Aggregated proteins often have an elongated, fibrous shape,^{7,8} and the response of particle counting and sizing instruments to non-spherical shapes has not been addressed extensively. Lloyd⁹ used a large-scale model of an ESZ orifice with particles made of modeling clay to illustrate the effect of shape. He found that for a fixed shape, particles of different sizes produced resistance changes proportional to the volume, but that the proportionality constant was different for different shapes. For cylinders with diameter/length ratios of 1 and 7, the signals differed by a factor of 3.44. Kachel¹⁰ also used a model orifice to compare the effects of the orientation of ellipsoids and discs as they pass through the orifice. He also performed measurements on blood cells in a custom ESZ system. He observed electrical pulse signals with three peaks, which was attributed to a rotation of the cell when passing through the orifice. Ferreira et al.¹¹ compared sieved (for size selection) beads, crushed glass, and mica with ESZ, light scattering, and sedimentation

Correspondence to: Richard Cavicchi (Telephone: +301-9753970; Fax: +301-9752643; E-mail: rcavicchi@nist.gov)

Journal of Pharmaceutical Sciences, Vol. 104, 971–987 (2015)

© 2014 Wiley Periodicals, Inc. and the American Pharmacists Association

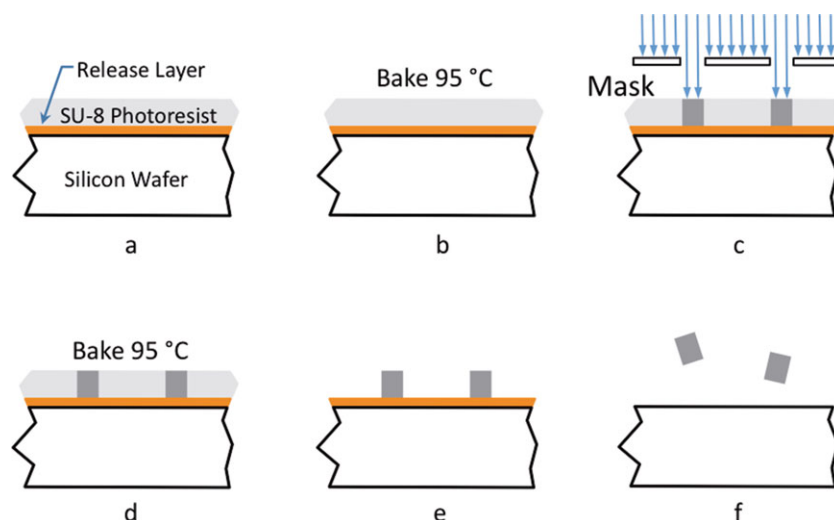


Figure 1. Schematic representation of fabrication process. (a) Coat wafer with release layer and SU-8, (b) pre-exposure bake at 95°C for 2 min, (c) expose wafer to UV light through mask to crosslink exposed SU-8, (d) post-exposure bake at 95°C for 2.5 min, (e) dissolve unexposed SU-8, and (f) dissolve release layer which releases particles into solvent.

measurements. Although the size distributions for ESZ and sedimentation were similar for the various particle types, the light scattering method reported substantially larger average particle diameter for the crushed glass and mica samples. Shekunov et al.¹² characterized particles of silica, zinc oxide, salmeterol xinafoate, and acetaminophen, each with a characteristic shape using time-of flight, light scattering, and ESZ instruments and found significant differences between the techniques for nonspherical shapes.

In the interest of resolving differences in size and concentration reported by different orthogonal size characterization methods and also with a motivation to improve measurements where possible, we have investigated the effect of particle shape on the measurements from these instruments. We have micro-fabricated particles of custom shapes as potential shape reference particles. Rods and disks were fabricated with the goal of accentuating the effects of particle shape, rather than to mimic the distributions present in a given sample of protein aggregates. Using finite element computation software, we have built models of orifices typical of commercial ESZ instruments and particles of defined size and shape. The models produce time-dependent trajectories for the flow and simulate electrical pulse signals that the ESZ instrument would produce. The results from all instruments indicated that particle shape has a significant influence on the reported size parameter. To investigate the effects in further detail, a microfluidic device was constructed that allowed for simultaneous measurement of the ESZ signal and collection of an associated optical image when the device was mounted in a microscope. Strobe photography was used to observe particle trajectories and their influence on the electrical signal.

EXPERIMENT

Particles of customized shape and size were fabricated using photolithography as schematically illustrated in Figure 1. An epoxy-based negative photoresist SU-8 (MicroChem Corporation, Newton, MA)¹³ was deposited by spinning it over a thin

release layer onto a silicon wafer. The thickness of the SU-8 depended on both the spin speed and formulation. For example, to produce a 2.5 μm thick layer, SU-8 2002 was used at a spin speed of 1800 revolutions per minute. The SU-8 was exposed to ultraviolet light through a mask and baked to selectively polymerize the particles. Unexposed SU-8 was removed in a solution of developer. Figure 2 shows an optical micrograph of a portion of the wafer at this stage. The wafer was then separated into 1.5 \times 1.5 cm^2 die, each containing a group of particles. The die were then placed in conical bottomed vials filled with photoresist remover. The remover dissolved the release layer and the the particles were now suspended in solution. The silicon die was removed and the vial of suspended particles was then placed in a styrofoam container overnight to suppress temperature gradients and resulting convection currents. The released particles settled to the bottom of the cone and formed a pellet. Once settled, the solvent was removed by gently pipetting out nearly all of the liquid and replacing it with ultrapure deionized water. Solvent exchange was performed three times to remove the solvent. If the particles were to be used in an ESZ device, Isoton II electrolyte solution (Beckman Coulter, Inc., Danvers Massachusetts) was added in the last exchange instead of water. To keep microbes from growing in the vials, sodium azide was added at a mass fraction of 0.05%. Nominal concentrations were 1000 particles/mL. SU-8 is hydrophobic with a contact angle of 80°.¹⁴

Particles were imaged and sized using a Zeiss NVision 40 field emission scanning electron microscope (SEM) detecting secondary emission electrons. Rod-shaped particles of nearly square cross section (referred to as rods hereafter) were dispersed onto an SEM substrate, as shown in Figure 3 for rods of nominal length 40 μm . Images (a) and (b) were imaged at 45° angle with respect to the substrate. Dispersed rods were either resting parallel to the orientation in which they were fabricated as in Figure 3a or resting on a side, at a right angle to the fabrication orientation as in Figure 3b. Thus, for a given rod it was possible to measure either the thickness or width along with the length. Images were collected from 14 particles of each size using a top view as in Figures 3c and 3d. Particle

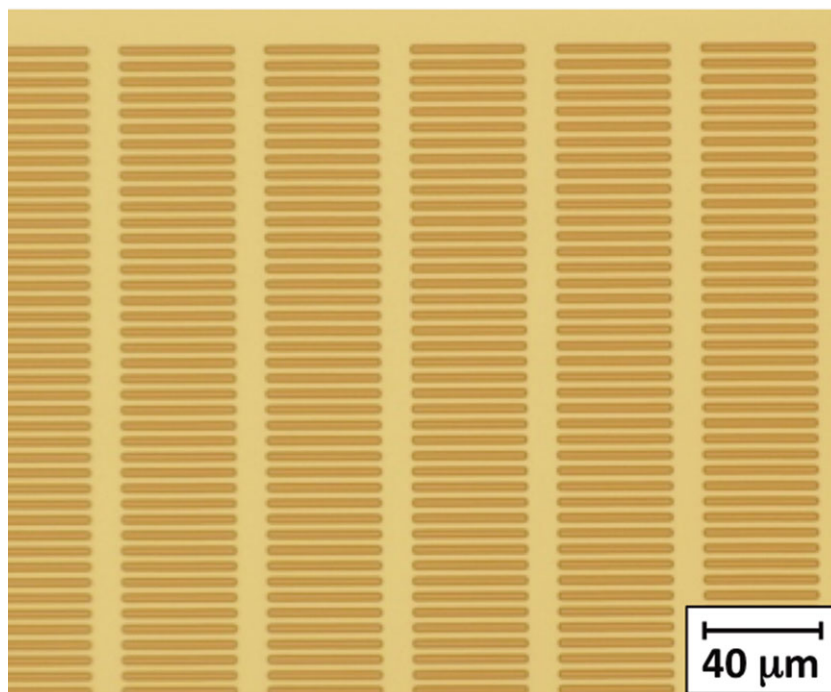


Figure 2. Optical image of a portion of a wafer with SU-8 rods.

dimensions were averaged and are presented in Table 1. The particle dimensions were used to calculate an ECD. To calculate the expected ECD for FI, it was assumed that the imaged rod would present as a rectangle with one dimension as the length of the rod l and the second dimension a width that would depend on the rotation of the rod about the rod's long axis. This dimension could range from the thickness of the rod to the square root of the sum of the squares of the thickness t and width w of the rod. The average ECD was obtained by integrating over all possible rotations about the rod's long axis. The dimensions in Table 1 for the nominal $30\text{ }\mu\text{m}$ rods account for the significant rounding of the ends of the rod. In addition to the rods, a set of disks was made with $49.6\text{ }\mu\text{m}$ diameter, and $3.6\text{ }\mu\text{m}$ thickness. The disks were used for measurements in the microfluidic ESZ device.

To compare the instrument performance on spherical particles, a set of samples were made using Aperture Instrument CC Calibrator beads added to Isoton II electrolyte solution. These samples have diameters traceable to NIST SRM 1960. Polystyrene beads of nominal diameter (and concentration) of $5\text{ }\mu\text{m}$ (20,000 per mL), $10\text{ }\mu\text{m}$ (10,000 per mL), $20\text{ }\mu\text{m}$ (10,000 per mL), and $40\text{ }\mu\text{m}$ (7000 per mL) were used.

Electrical sensing zone measurements were performed using both our microfluidic device and a commercial ESZ instrument. The commercial instrument was a Beckmann-Coulter multisizer 4 using a $70\text{ }\mu\text{m}$ diameter orifice. The instrument analyzed a volume of 1 mL for each run at a flow rate of $21\text{ }\mu\text{L/s}$. Three measurements were made for each condition.

The microfluidic ESZ chip consisted of a microchannel with four Au electrodes. The electrodes were deposited on a glass slide and consisted of a 100 nm indium tin oxide adhesion layer and 200 nm thick Au patterned by photolithography. The microchannel was formed in polydimethylsiloxane (PDMS) (Sylgard 184; Dow Corning) by a process illustrated in Figure 4.

SU-8 2050 (MicroChem Corporation) was spun to a thickness of $60\text{ }\mu\text{m}$ and patterned into the reverse of the microchannels and access ports. This produced a reusable master mold which can be used to create many PDMS devices. Figure 4a shows a section of the SU-8 structure over which PDMS was poured to create the microchannel. Figure 4b shows an optical image of the microchannel master. The PDMS base and curing agent mixture (ratio 10:1 by weight) was poured over the master to a thickness of 3 mm and cured at $80\text{ }^{\circ}\text{C}$ for 2 h as shown in Figure 4c. The cured PDMS was peeled from the master (Fig. 4d), and cut into individual devices (Fig. 4e). The PDMS was then treated with an oxygen plasma to chemically activate the surface prior to bonding. The activated PDMS was aligned with electrodes (Fig. 4f) on the glass slide and pressed to bond to the glass slide (Fig. 4g). The final step was an overnight bake at $80\text{ }^{\circ}\text{C}$. Figure 5 shows three images of the completed device at different magnifications.

The fabricated ESZ chip was mounted in a fluorescence/optical microscope (Fig. 6a). The microscope was outfitted with a Basler scA1390–17fm CCD camera and with a 470 nm light emitting diode (LED) (Luxeon-Star LXML-PB01–0030) as a light source. A voltage (typically 8–16 V) was applied between the outer electrodes (shown in Fig. 5b). The voltage between the inner electrodes was measured with an Ithaco 1201 differential pre-amplifier. The output signal was further amplified with an operational amplifier in a custom electronic circuit. This signal was measured using a National Instruments PCIe-6361 card. Image acquisition, data acquisition, and data analysis were under computer control using LabVIEW together with the LabVIEW Vision Development Module. Flow was established using a syringe pump, which was operated at $40\text{ }\mu\text{L/s}$ in the measurements reported in this paper. The microchannel featured an ESZ between the two inner electrodes, where the channel width was reduced. When a particle entered this zone,

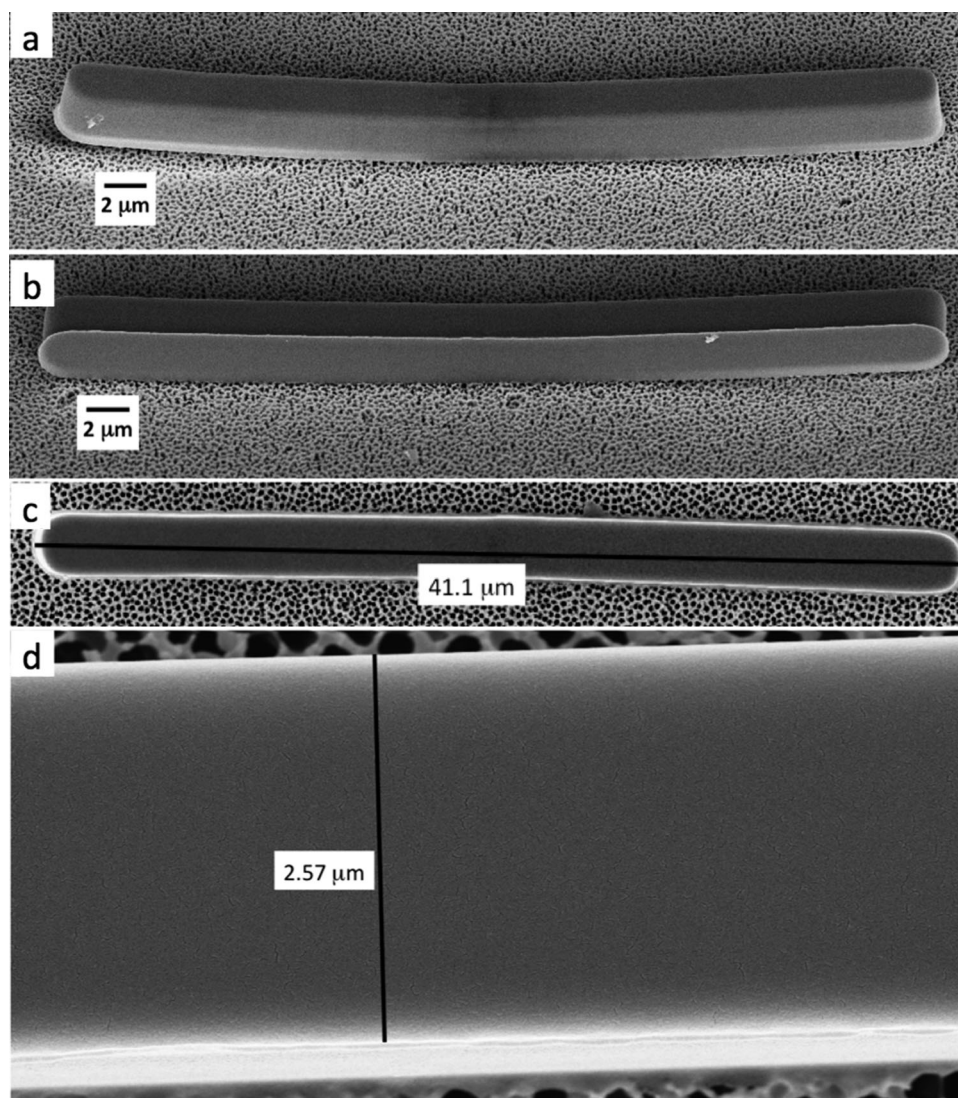


Figure 3. Measurement of rod dimensions. Rods were dispersed onto a SEM substrate; shown here are rods of nominal length 40 μm . Images (a) and (b) are imaged at 45° angle with respect to the substrate. Dispersed rods were either resting parallel to the orientation in which they were fabricated as in (a) or resting on a side, at a right angle to the fabrication orientation (b). (c) and (d) are top view images of the rod in (a) with dimensions indicated.

Table 1. Dimensions of Microfabricated Rods Measured using Scanning Electron Microscopy

| Nominal Length (μm) | Length (μm) | Width (μm) | Thickness (μm) |
|----------------------------------|--------------------------|-------------------------|-----------------------------|
| 30 | 31.6 ± 0.3 | 6.6 ± 0.2 | 4.5 ± 0.2 |
| 40 | 41.4 ± 0.2 | 2.80 ± 0.07 | 2.57 ± 0.02 |
| 50 | 51.14 ± 0.2 | 3.43 ± 0.04 | 2.57 ± 0.02 |

the electrical signal triggered the exposure of the cameras. The timing sequence is indicated in Figure 6b. A controlled delay with microsecond resolution was used to trigger the flash of the LED which lasts typically 5 μs . The camera produced an image which was correlated with the electrical signal. Both camera images and electrical signals were stored for each particle analyzed. By use of multiple flashes during a single exposure, a strobe-like image was obtained of the particle's trajectory through the microchannel.

Light obscuration measurements were made with a PAMAS SVSS-C (Partikelmess- und Analysesysteme GmbH, Rutesheim, Germany) equipped with an HCB-LD-25/25 sensor. Three measurements of a volume of 0.3 mL of each sample were performed with a pre-run volume of 0.5 mL at a fixed fill rate, emptying rate, and rinse rate of 10 mL/min. A test was made with 50 μm rods at a flow rate of 25 mL/min to test for any affect of flow rate on the size distribution, but the distributions were similar. The mean particle concentration per milliliter was reported by the system. Samples were measured in triplicates and mean and standard deviation were calculated.

Flow imaging measurements were made using two instruments. Instrument A was a DPA-4200 (ProteinSimple, Santa Clara, California) with an SP3 setup. Samples were analyzed with a sample volume of 0.5 mL (analyzed volume 0.44 mL or 84% sampling efficiency) and a pre-run volume of 0.2 mL at a flow rate of 0.1 mL/min. Particle parameters were calculated using the MFI view application software version 1.3. Image

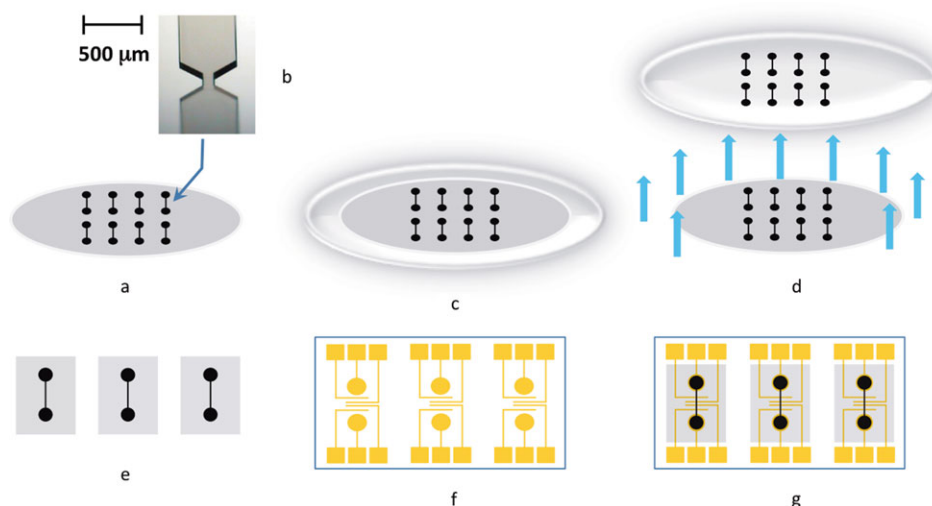


Figure 4. Microfluidic ESZ chip fabrication steps: (a) Create master from SU-8 on a silicon wafer, (b) microscope image of SU-8 master showing restriction in the center of the channel, (c) cover wafer with PDMS, (d) remove PDMS layer, (e) cut out individual PDMS microfluidic channels, (f) fabricate gold electrodes on a glass slide, and (g) attach PDMS microfluidic channels to electrode slide and the device is completed.

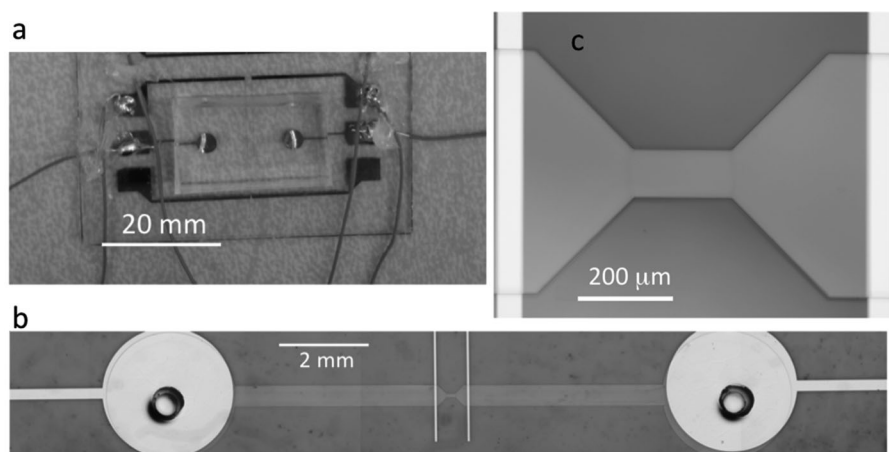


Figure 5. Microfluidic ESZ chip. (a) View of chip with wires connecting electrodes. (b) Zoomed image (made from stitching together three photos taken in an optical microscope) showing ports for inlet and outlet (on left and right), the two electrodes for applying voltage to the channel (large circles) and the pair of electrodes for measuring the differential voltage across the constriction in the microchannel. (c) Further zoomed optical micrograph showing the constriction and electrodes on either side.

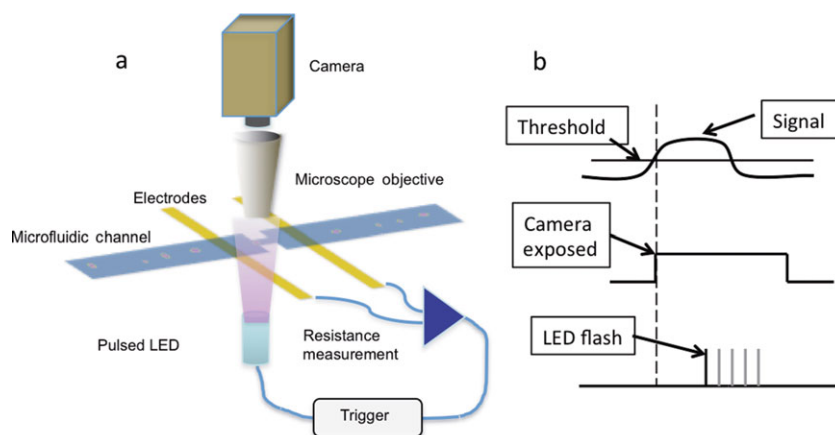


Figure 6. (a) Schematic representation of microfluidic ESZ measurement. (b) Sequence for operation of the ESZ chip to acquire pulse signal and images of a particle in the sensing zone.

data files were stored as PNG files. Instrument B was a Flow-CAM (Fluid Imaging Technologies Inc., Yarmouth, Maine) with a 100 μm flow cell and a 10 \times microscope objective. The camera operated in auto image mode at 15 frames per second, with an efficiency of 10.8%. Image data files were stored as TIF files. Three samples were measured for each particle type. Comparison of the use of these two instruments has been discussed by Wilson and Manning.¹⁵ Upon completion of a run, images of particles that were rods were selected using the software filter tools or manual selection for further analysis.

Instrument A sets a threshold for determining which pixels are part of a particle. It then sums the number of pixels and converts to an area. An equivalent diameter that is equal to the diameter of a circle with the same area is calculated. To account for the finite optical resolution of the instrument, which is a consequence of optical diffraction, a constant value is subtracted to produce the reported ECD. Instrument B allows the user to set a threshold for how different a pixel brightness is from a calibration image collected at the beginning of a run. The threshold difference can be either positive (light), negative (dark), or a combination of thresholds for light and dark.

Finite element calculations modeling ESZ were performed using COMSOL Multiphysics with the AC/DC Module. Figure 7 shows an example of an orifice separating two chambers of much larger volume with the inclusion of a rod-shaped particle in the orifice. The conductivity of the particle was set equal to zero, while the conductivity of the environment was set to the value of Isoton II, the saline solution used in our ESZ instrument. The orifice had dimensions of 70 μm diameter, 77 μm length. The orifice was modeled as opening into a cylinder on either side of diameter 250 μm and length 500 μm . The resistance between opposite faces was calculated with the particle located at different positions along the axis running through the center of the orifice. Models were obtained for rods of the same dimensions as used in experiments and for spheres of equal volume. Calculations were made for rod orientation with respect to the flow axis at 0°, 45°, and 90°.

NOMENCLATURE

Particle measurement instruments infer particle diameter from measured particle properties.

Electrical sensing zone measurements nominally measure the volume of liquid displaced by a particle and report the diameter as the ESD of a sphere of the same volume. LO measures the amount of light scattered from a particle and reports the particle diameter as the particle of a polystyrene latex sphere with the same scattering strength. For irregular particles such as protein aggregates, neither the ESZ nor the LO diameter definitions are directly related to the dimensions of the periphery of the particle. The volume of the rods measured in this work can also be inferred from SEM measurements of length, width, and thickness, and we use ESD to denote the diameter of a sphere of the same volume as the volume inferred from the SEM measurements.

Flow imaging infers particle diameter from the projected area of particles as captured by electronic optical images. Instrument A reports an ECD equal to the diameter of a circle that has the same area as the projected area of the particle, after filling any holes in the particle. Instrument B reports diameter as Area Based Diameter (ABD, either with or without filling of holes), or as average of the feret diameter over 36 angles. Instrument B refers to the feret-based diameter as an ESD, but to avoid confusion with the use of ESD to describe the volume-based diameters, we use the term average feret diameter (AFD) in this paper.

RESULTS

Summary of Results for Particle Size and Count

Table 2 shows a comparison of results from polystyrene calibrator beads prepared in Isoton II electrolyte. The diameter reported for the FI methods is an ECD, whereas the diameter reported for ESZ is an ESD. There is agreement within ten percent on the number and size of the beads between the different methods, except for the 5 μm bead where Instrument B reports a larger ECD than the other methods. In the measurements in Table 2, flow instrument B was set with a threshold for dark pixels only (instrument parameter 15). The results for the microfabricated rods of nominal length 30, 40, 50 μm are summarized in Table 3. This table also includes the length (reported by Instrument A) and maximum feret diameter and AFD (reported by Instrument B). For each set of collected data using Instrument B, the images were processed using a

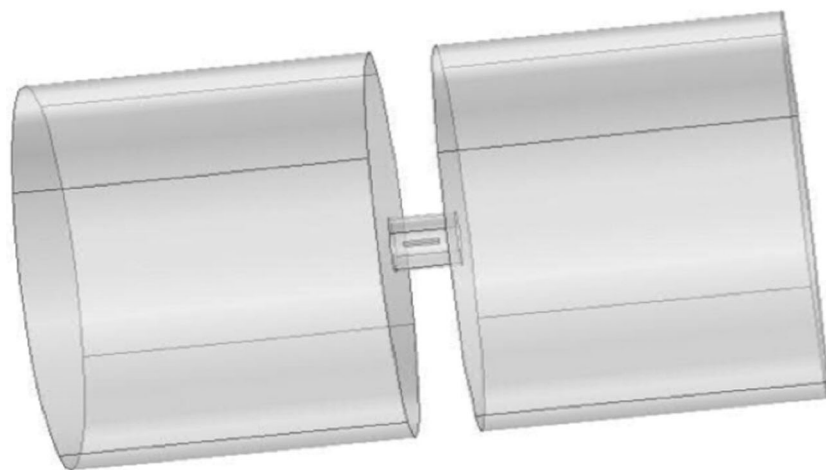


Figure 7. COMSOL model of orifice with rod aligned with flow direction.

Table 2. Measured Particle Parameters for Different Instruments for Polystyrene Beads

| Nominal Dimension | ESZ (Multisizer) | | FI Instrument A | | FI Instrument B | | LO | |
|-----------------------|-----------------------|--------------------------|-----------------------|--------------------------|-----------------------|--------------------------|-----------------------|--------------------------|
| d (μm) | d (μm) | N (mL^{-1}) | d (μm) | N (mL^{-1}) | d (μm) | N (mL^{-1}) | d (μm) | N (mL^{-1}) |
| 5 | 5.27 | 18,672 | 5.20 | 20,893 | 6.45 | 20,039 | 5.50 | 19,345 |
| 10 | 10.6 | 9468 | 10.0 | 10,337 | 10.9 | 9433 | 10.0 | 10,514 |
| 20 | 20.2 | 10,320 | 18.9 | 10,063 | 21.0 | 9930 | 19.0 | 10,282 |
| 40 | 40.1 | 6288 | 38.1 | 7358 | 40.4 | 7343 | 37.5 | 6809 |

Table 3. Measured Particle Parameters for Different Instruments for 30, 40, and 50 μm Rods

| Method | Length (μm) | Maximum Feret Diameter (μm) | ECD (or ABD) (μm^2) | Mean Feret Diameter (μm) | ESD (μm) | Volume (μm^3) | Aspect Ratio |
|--|--------------------------|--|----------------------------------|---------------------------------------|-----------------------|----------------------------|--------------|
| SEM | 31.6 | 32.4 | 16.2 | 15.0 | 11.9 | 896 | 0.22 |
| LO | | | 9.9 | | | | |
| FI Instrument A | 27.7 | | 17.3 | | | | 0.4 |
| FI Instrument B | | 34.9 | 22.5 | 26.3 | | | 0.4 |
| FI Instrument B, (dark threshold only) | | 33.6 | 16.7 | 22.8 | | | 0.26 |
| ESZ (Multisizer) | | | | | 11.7 | 838 | |
| SEM | 41.4 | 41.6 | 13.4 | 10.28 | 8.3 | 298 | 0.082 |
| LO | | | 6.45 | | | | |
| FI Instrument A | 37.7 | | 17.9 | | | | 0.22 |
| FI Instrument B | | 43.85 | 21.34 | 31.17 | | | 0.24 |
| FI Instrument B, (dark threshold only) | | 41.40 | 15.24 | 27.82 | | | 0.14 |
| ESZ (multisizer) | | | | | 7.65 | 234 | |
| SEM | 51.1 | 51.2 | 15.93 | 11.75 | 9.6 | 459 | 0.073 |
| LO | | | 7.4 | | | | |
| FI Instrument A | 47.7 | | 20.1 | | | | 0.19 |
| FI Instrument B | | 53.7 | 25.3 | 37.8 | | | 0.22 |
| FI Instrument B, (dark threshold only) | | 41.40 | 15.24 | 27.82 | | | 0.14 |
| ESZ (multisizer) | | | | | 8.68 | 342 | |

threshold based on dark pixels only (instrument parameter 12), and light and dark pixels (instrument parameters 8 and 12, respectively). Calculated values of these parameters based on the SEM measurements are also included. These calculations assume the axis of the rod is in the plane of the flow cell but with a rotational average of the width and thickness dimensions. The calculated AFD begins with a rectangle of dimensions equal to the length and rotational average of the width and thickness. From this, the feret dimension is calculated for 36 uniformly spaced angles (separated by 5°) and an average is taken of the results.

Electrical Sensing Zone

Figure 8 shows histograms from ESZ measurements on microfabricated rods. The red arrow in the figure corresponds to the ESD that would be calculated from the SEM-measured dimensions of the rods. Compared with the more elongated 40 and 50 μm rods, the wider 30 μm rods resulted in a broader distribution of size, with a mean size that exceeded the actual ESD. By contrast the 40 and 50 μm rods produced a narrower size distribution whose mean size was below the actual ESD. The histograms consistently showed two peaks which may result from different preferred orientations of the rods passing through the orifice. Figure 9a shows a COMSOL calculation of

the resistance change obtained for a 70 μm orifice when a rod of the same dimensions as the 40 μm rod used in the experiments passes through three different orientations, and also an equivalent volume sphere of diameter 8.30 μm . When the rod passes through with its long axis parallel to the direction of flow, the electrical signal's amplitude is reduced by 30% compared with the signal produced by an equivalent volume sphere. A reduction in signal by this amount would convert to an instrument reported diameter of 7.35 μm . Thus, if all of the rods pass through with their axis aligned, with the flow direction, the instrument would report an ESD that is 1 μm less than the actual ESD of the particle. A particle traveling at 45° with respect to the flow contributes a signal that would yield an ESD equal to the particle's actual ESD. Figure 9b shows the effect of size for a fixed rod shape. For the calculation in this figure, all dimensions of the 40 μm rod were scaled by the same scaling factor α , with $\alpha = 1$ representing the case of the 40 μm rod. Results are shown for 0° , 45° , and 90° . It is evident from the log-log plot that differences in signal amplitude for the three orientations scale by factors that are independent of the rod size. Maps of the current density for a rod at 0° and 90° are shown in Figure 10 for the three orthogonal planes that intersect the center of the orifice. For the 40 μm rods, the measured median value of 7.65 μm (Table 3) is generally consistent with most particles

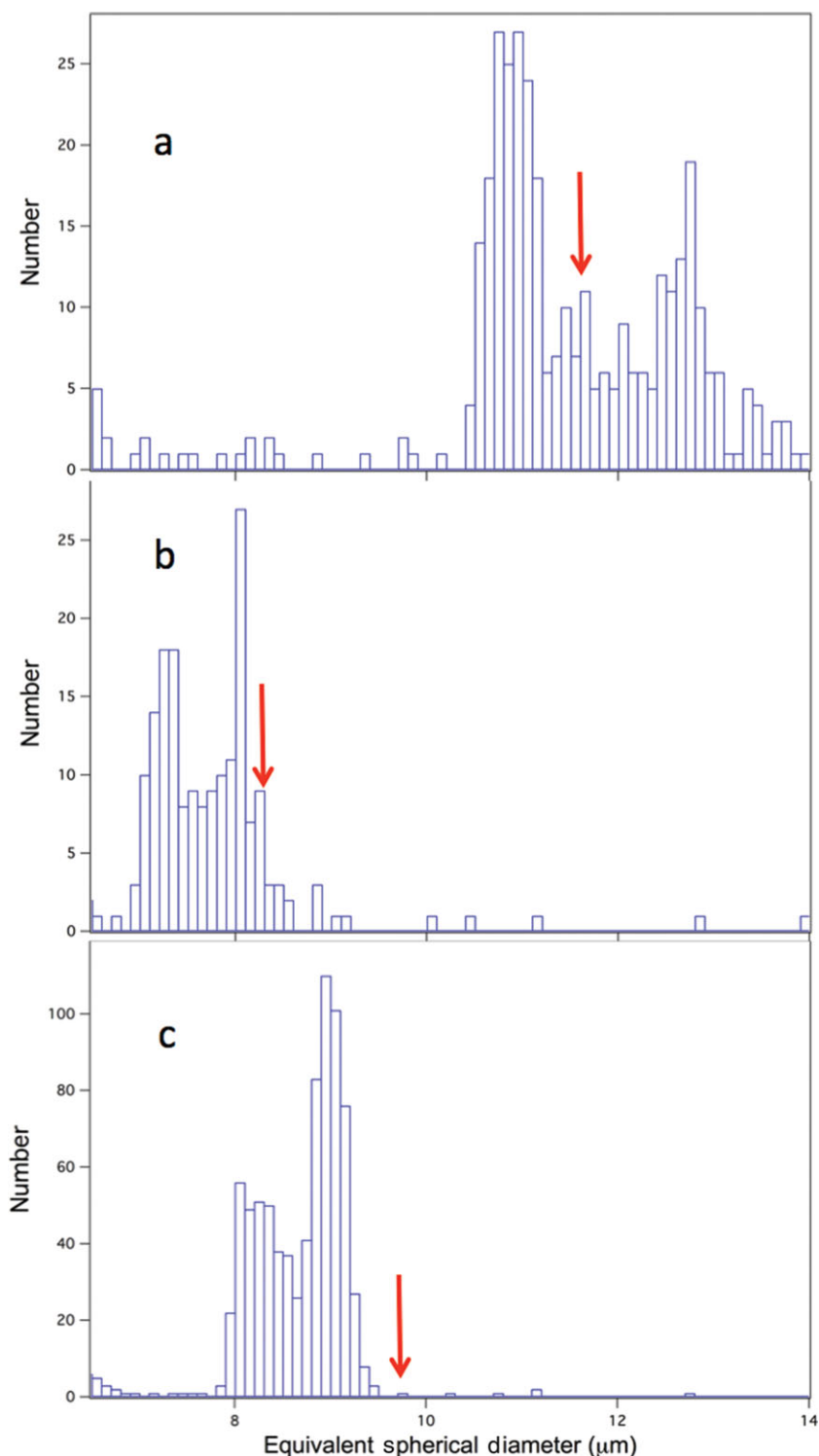


Figure 8. Electrical sensing zone data from rods of dimensions (a) $31.6 \times 6.6 \times 4.5 \mu\text{m}^3$, (b) $41 \times 2.8 \times 2.6 \mu\text{m}^3$, and (c) $51 \times 3.4 \times 2.6 \mu\text{m}^3$. Red arrow indicates equivalent spherical diameter based on dimensions of the rods measured in an SEM.

aligning with the flow direction. Figure 10 shows COMSOL calculations of the current density map for 0° (aligned with flow) (Fig. 10a) and 90° (perpendicular to the flow) (Fig. 10b). This illustrates the effects of reduced pathways for electrical current when the rod is perpendicular to the flow direction giving rise to a higher electrical resistance.

The microfluidic ESZ chip was used to perform simultaneous measurements of FI and ESZ and further elucidate the effects observed in the commercial instrument. For the results presented here, the system was run in strobe mode, with multiple flashes of the LED equally spaced in time for each exposure of a particle. An example is shown in Figure 11 where the spacing

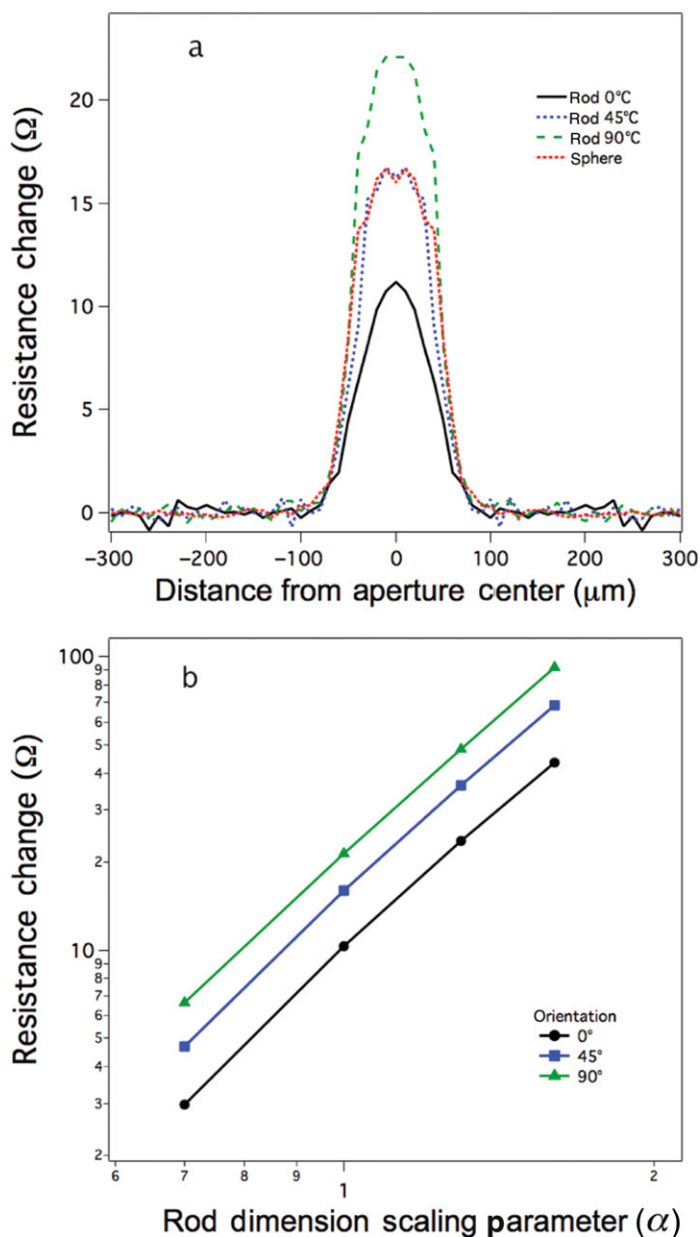


Figure 9. (a) Model of resistance change versus position for sphere diameter $8.3 \mu\text{m}$ (dashed red line); rod with dimensions $41 \times 2.8 \times 2.6 \mu\text{m}^3$ aligned with orifice axis (solid black line); and a rod of the same dimensions at an angle of 45° with respect to the orifice axis (dotted blue line), and an identical rod at an angle of 90° with respect to the orifice axis (dashed green line). The sphere of diameter $8.3 \mu\text{m}$ has the same volume as the rod. For all cases, the particle is flowing through the center of the orifice. The total resistance of the modeled structure in absence of a particle was $22.46 \text{ k}\Omega$. (b) Effect of particle size for fixed shape scaled by a parameter α in all three dimensions. $\alpha = 1$ corresponds to a $41 \times 2.8 \times 2.6 \mu\text{m}^3$ rod. Model of resistance change versus α is plotted for three different orientations of the rod with respect to the orifice axis.

between flashes was $300 \mu\text{s}$. In Figure 11a, a $20 \mu\text{m}$ polystyrene bead travels down the center of the microchannel, whereas in Figure 11b, a $20 \mu\text{m}$ bead travels along the edge of the microchannel. The corresponding signals are shown below each micrograph. The particle takes longer to travel along the edge

through the active zone due to the parabolic velocity profile of flow in a channel. This is apparent in the optical images, where there is a closer spacing of the appearances of the particle in the edge trajectory image (Fig. 11b) compared with the center trajectory image (Fig. 11a). Correlated with this imaging observation, the electrical pulse signal is also wider for the edge trajectory particle. In addition, the particle flowing along the edge has a distinctive pulse shape, with maxima occurring as the particle enters and exits the sensing zone. This pulse shape was typical of all particles traveling close to the edge. The microfluidic ESZ device was modeled in COMSOL with the results shown in Figure 12. The peak shapes for center and edge trajectories are similar to those observed experimentally. These results are consistent with and elucidate the work of Berge et al.¹⁶ who assumed parabolic flow velocity, used the pulse-width to compute a radial position for particles in a $570 \mu\text{m}$ long pore, and then associated an increase in pulse amplitude with radial offset.

Example images from the $30 \mu\text{m}$ rod and $50 \mu\text{m}$ disc flowing through the ESZ are shown in Figures 13 and 14. In Figure 13a, the rod appears to pass with its long axis aligned with the flow, whereas in Figure 13b, the particle changes orientation or “tumbles” through the ESZ. Tumbling of rods occurs when the rod is located in a region of fluid shear, and has been previously observed for small rods flowing in a 2.5 mm channel at speeds 1000 times slower than in the present experiments.¹⁷ The timing of the maximum signal in Figure 13b corresponds to the fourth image of the particle in Figure 13b where the particle is observed to have the greatest rotation from on-axis flow of the five images superimposed by the strobe photograph. Comparing the signals in Figures 13a and 13b, it is clear that the on-axis flow results in a smaller signal, about 1/2 the signal from the signal at the moment of perpendicular orientation in Figure 13b. This is very similar to the COMSOL calculation in Figure 9a for parallel and perpendicular orientations. The correlation of the moment of maximum tumbling and maximum electrical signal is even more dramatic for the case of the disk in Figure 14. The superposition of a narrower peak over a broader peak was typical of the vast majority of tumbling events observed and indeed serves as clear evidence of tumbling.

The likelihood of tumbling depended on the aspect ratio of the particle. Figure 15 shows a comparison of histograms from $30 \mu\text{m}$ (Fig. 15a) and $40 \mu\text{m}$ rods (Fig. 15b). Resistance change was strongly correlated with whether or not the rods tumbled as shown by the fraction of rods tumbling in each size bin indicated by the solid red circles. The $40 \mu\text{m}$ rods because of their longer shape (Table 1) had a stronger tendency to align with the flow than the $30 \mu\text{m}$ rods. This resulted in a narrower distribution of measured resistance changes compared to the $30 \mu\text{m}$ rods which have a larger width to length ratio. The arrows in the figure represent the resistance change that would be measured by a sphere of an equivalent volume to the rod. Note that the tumbling flow of the shorter and wider $30 \mu\text{m}$ rods produced resistance changes that are larger than the equivalent sphere. These results are in agreement with the results observed with the commercial instrument (Fig. 8) and indicate that particle shape influences tumbling probability and this in turn influences the signal amplitude and size reported by ESZ. It was found that the flow rate in the microchannel when varied from 30 to $80 \mu\text{L/s}$ had little effect on the histograms or fraction of particles observed to tumble.

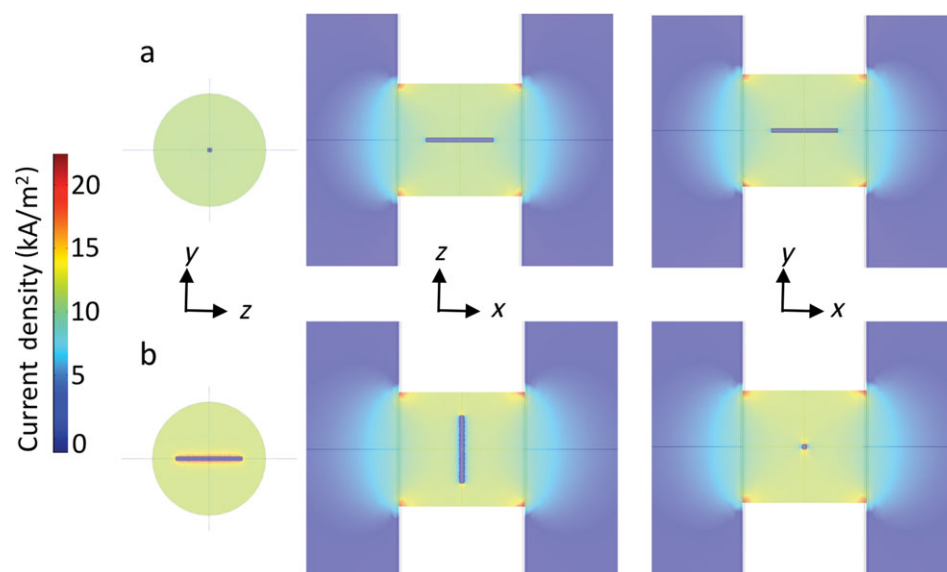


Figure 10. COMSOL map of current amplitude for a rod passing through the center of the orifice for with the rod is (a) parallel to the axis of the orifice and (b) perpendicular to the axis of the orifice. Three orthogonal planes passing through the center of the orifice are shown for each orientation of the rod.

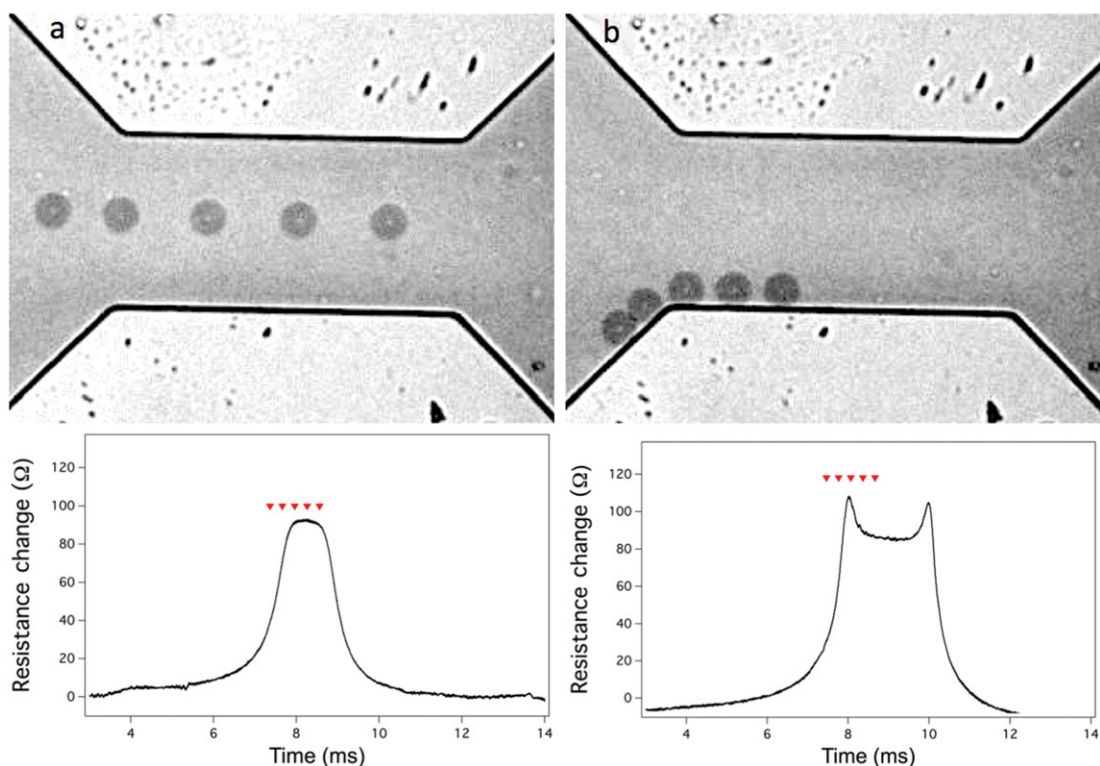


Figure 11. Images and signal from 20 μm diameter bead traveling down (a) the center of the sensing zone of the microfluidic ESZ chip, and (b) along the lower edge of the sensing zone. Flow is from left to right in the image. Red triangles in graph indicate the times of the diode flash with an interval of 310 μs .

Light Obscuration

Light obscuration results are shown in Figure 14 for the 40 μm rods. The histogram also showed two peaks.

Provided that the refractive index of a particle exceeds that of the matrix liquid by at least ≈ 0.2 and the smallest dimension of a particle is much larger than the wavelength of light, the

amount of scattered light depends only on the projected area of the particle.¹⁸ The rods studied here meet these criteria: the refractive index of SU-8 (≈ 1.6) is 0.27 higher than water, and the rod width of 2.7 μm substantially exceeds the wavelength of light in the water medium (0.50 μm). An exact calculation of scattering from a tumbling square rod with dimensions much

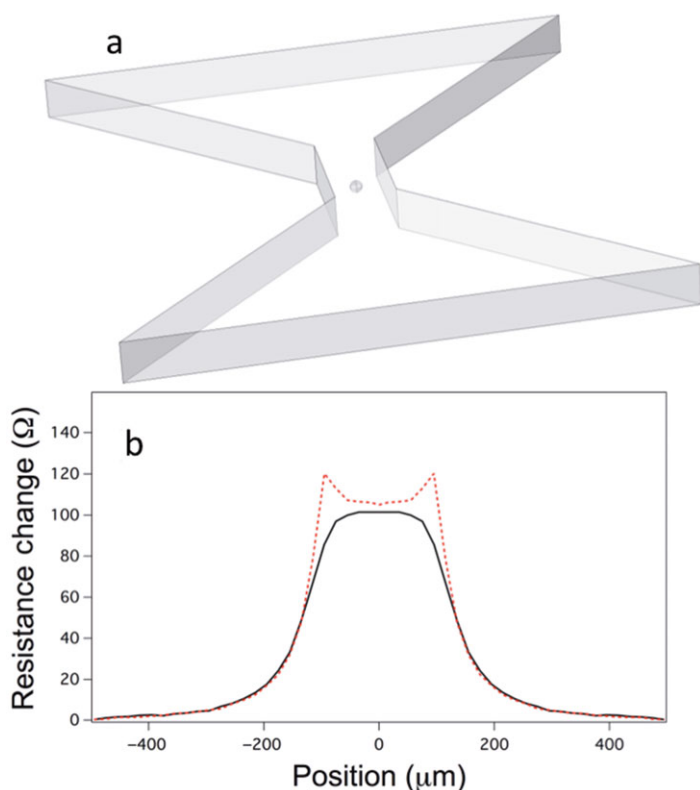


Figure 12. (a) COMSOL model of microchannel with 20 μm diameter bead in center of the sensing zone. (b) Model of resistance change versus position for sphere diameter 20 μm flowing down the center of the microchannel (solid black line) and flowing down the right side of the microchannel, offset by 37 μm from the center (dotted red line). The total resistance of the modeled structure in absence of a particle was 46.05 k Ω .

greater than the wavelength of light is very difficult. However, calculations of the light scattering of spheres,¹⁹ randomly oriented spheroids,²⁰ and of finite-length cylinders oriented perpendicular to the incident light²¹ confirmed that deviations of true scattering cross sections from the asymptotic limit produce shifts in reported diameter of $\approx -10\%$. In the limit of large particles with high refractive index, LO is a measure of the projected area of the particle, and not the particle volume, and the LO results can be interpreted by simply considering the variation in projected area of the rods as a function of the orientation of the rods with respect to the incident light beam.

The maximum projected area corresponds to a rod that is aligned with the flow and with the axial rotation of the rod chosen to maximize the apparent width of the rod. The projected area is then $(t^2 + w^2)^{1/2}$ and the ECD for the 40 μm rods is 14.2 μm . For rods that are tumbling, the average projected area can be obtained simply from a theorem that states that the projected area of a randomly oriented, convex particle is 1/4 of the surface area of the particle. For $l \gg w$, $l \gg t$ the surface area of the rods is approximately $2(w + t)l$. Thus, the average projected area is $(w + t)l/2$, giving an ECD of 11.9 μm . Applying the approximate -10% correction, we obtain 12.8 μm as the calculated maximum ECD and $\approx 11 \mu\text{m}$ as the calculated ECD for tumbling rods. The latter is indicated by a red arrow in Figure 16.

The minimum projected area corresponds to a rod that is aligned in the same direction as the laser beam, with an area of w^2 and an ECD for the 40 μm rods of only 3.0 μm . Only a small fraction of possible orientations can produce projected areas this small. Based on this observation and the observation that the average ECD for tumbling particles is only slightly smaller than the maximum ECD, we would expect the particle size distribution to be strongly asymmetric with a peak much closer to the maximum observed diameter than near the minimum diameter.

The observed particle size distribution, as shown in Figure 16, only partially conforms to these expectations. The measured distribution ranges from 2 to 10 μm , in approximate agreement to the expected range from 3 to 12.8 μm , but the measured distribution has two pronounced peaks near 5 and 8.5 μm instead of the expected single peak near 11 μm . The measured average ECD of 6.4 μm differs significantly from the expected average of 11 μm for randomly oriented rods or 12.8 μm for flow-aligned rods.

The significant undersizing implies that the rods are not scattering as much light away from the detector as a PSL bead of the same ECD. We have identified two possible causes of reduced light scattering.

First, if the rods are aligned in the flow field and the rod length exceeds the thickness of the illuminated volume in the flow cell, only part of the rod length will be illuminated at any point in time. As a result, the total scattering will be approximately proportional to the fraction of the rod that is illuminated. The PAMAS LO counter that was used has a very low coincidence error (the error in count caused by two particles simultaneously residing in the illuminated zone). The manufacturer states that the instrument has a 7.8% coincidence error at a particle concentration of 120,000 mL^{-1} . If one particle is detected in the illuminated zone, the probability of a second particle being detected may be obtained from the Poisson distribution. By adjusting the volume of the illuminated zone to give a 7.8% coincidence error, the estimated volume is 690,000 μm^3 . Assuming that the flow cell has a cross section of $250 \times 250 \mu\text{m}^2$, slightly larger than the 200 μm maximum detectable particle diameter, the thickness of the illuminated volume would be $\approx 11 \mu\text{m}$. An aligned rod would then scatter a fraction $(11 \mu\text{m})/(41.4 \mu\text{m}) = 0.27$ of the light that a bead of the same ESD scatters. (This scaling assumes that the bead diameter does not exceed the thickness of the illuminated zone, which is valid in the present case). In a size region where the extinction efficiency factor does not vary rapidly with diameter, indicated diameter scales as the square root of the total scattered light. The expected ECD for a partially illuminated, aligned rod is thus $\approx (0.27)^{1/2}(12.8 \mu\text{m}) = 6.6 \mu\text{m}$, which is close to the observed average ECD. It is plausible that the measured peak near 5 μm corresponds to partially illuminated, aligned rods, and the peak near 8.5 μm corresponds to tumbling rods that are more fully illuminated.

A second possible explanation for the data is that the diffraction of light from a thin rod aligned with the flow field is largely in a plane perpendicular to the rod axis. If a LO instrument is built with a detector aperture of the same narrow shape as the beam illuminating the flow cell, then this fan-shaped scattering will match the detector aperture very well. The result would be that less light would be scattered away from the detector than a spherical bead, which scatters light in a cone-shaped pattern. However, we have no direct

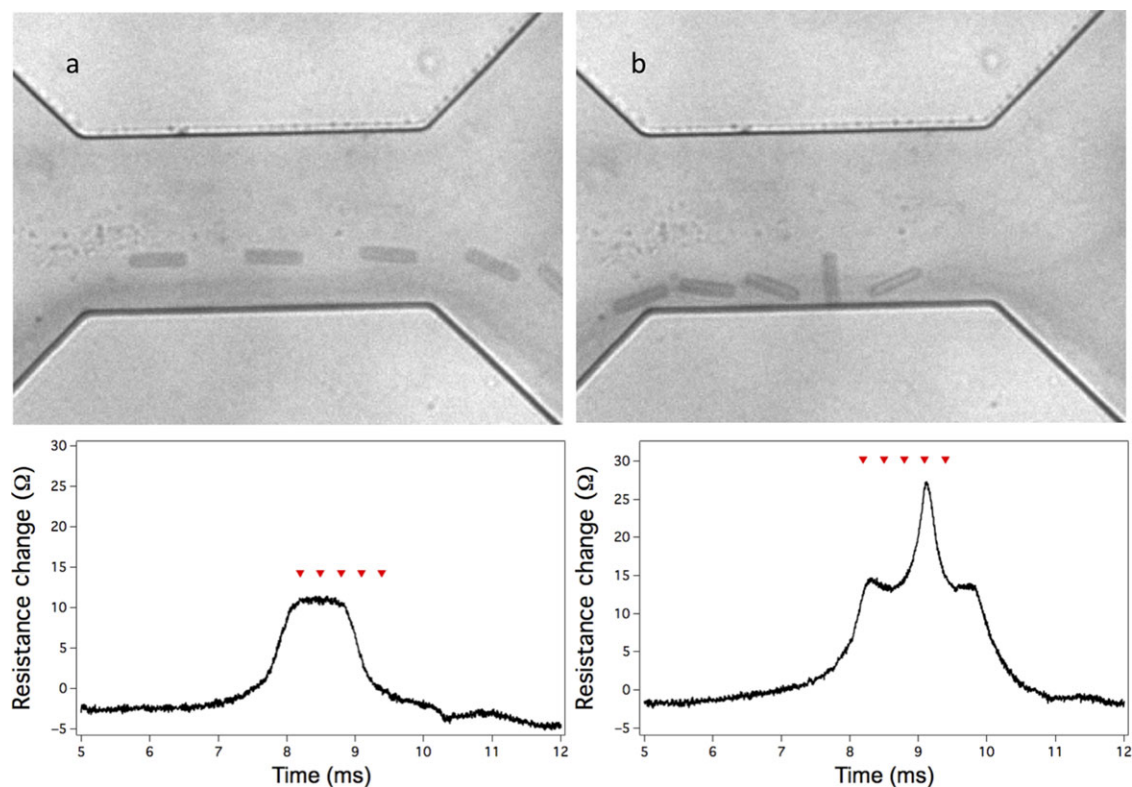


Figure 13. Images and signal from (a) non-tumbling and (b) tumbling rod of dimensions $32 \times 6.6 \times 4.5 \mu\text{m}^3$ in the microfluidic ESZ chip. Flow is from left to right in the image. Red triangles in graph indicate the times of the diode flash with an interval of $300 \mu\text{s}$.

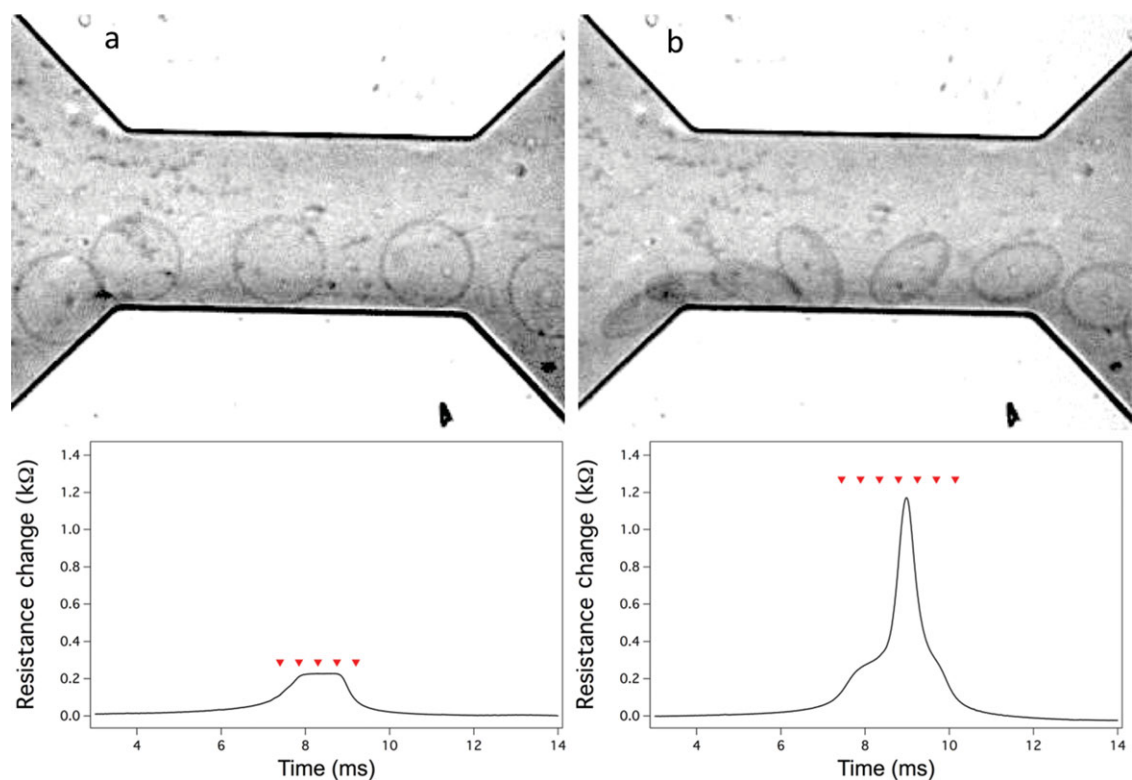


Figure 14. Images and signal from (a) non-tumbling and (b) tumbling $50 \mu\text{m}$ diameter, $5 \mu\text{m}$ thick disc in the microfluidic ESZ chip. Flow is from left to right in the image. Red triangles in graph indicate the times of the diode flash with interval of $440 \mu\text{s}$.

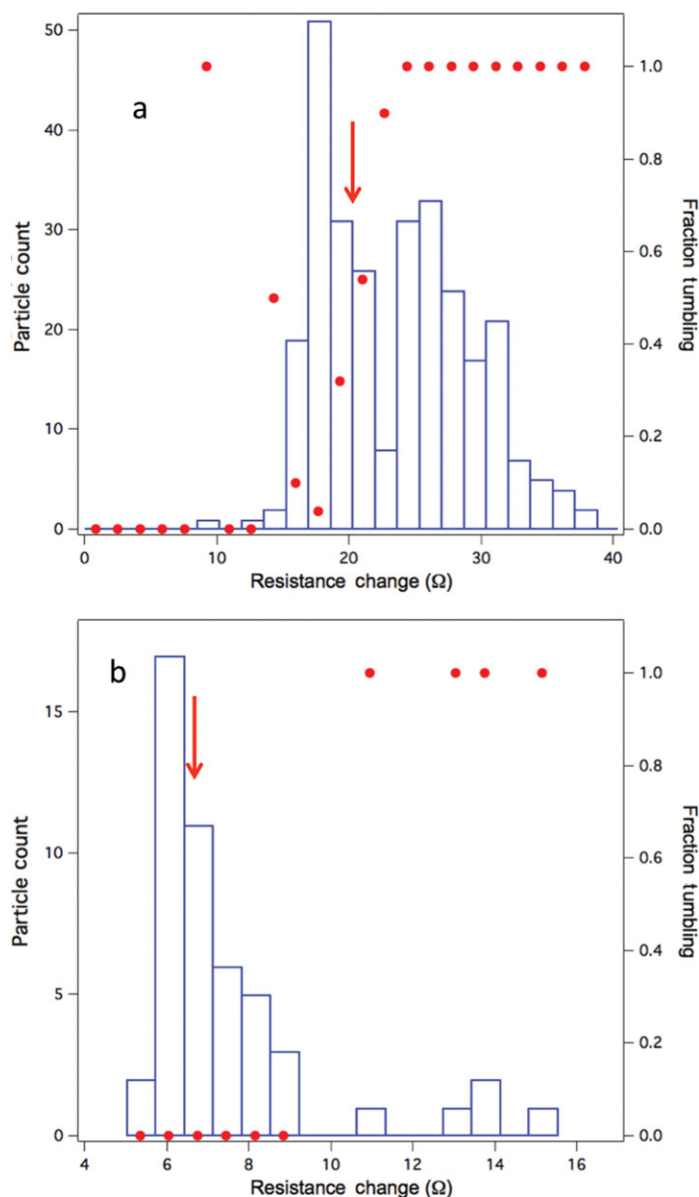


Figure 15. Histogram of measured resistance changes for rods of dimensions (a) $31.6 \times 6.6 \times 4.5 \mu\text{m}^3$, (b) $41 \times 2.8 \times 2.6 \mu\text{m}^3$, in the microfluidic ESZ chip. Solid red circles associated with the right axis indicate the fraction of rods in each histogram bin that were tumbling. The red arrow indicates the resistance change that would be obtained from an equivalent spherical diameter based on dimensions of the rods.

knowledge of the use of rectangular detector apertures in the PAMAS instrument.

Because the details of the light source, detector, flow cell, and optics geometry are all proprietary, a quantitative model of these effects is not possible. A full elucidation of these effects would additionally require building a combined LO and bright-field imaging system that could measure light scattering and particle orientation simultaneously.

Flow Imaging

Figure 17 shows images of the 40 μm rods obtained by the FI instruments. It is evident that in both instruments there was a strong tendency for the rods to align with the direction of

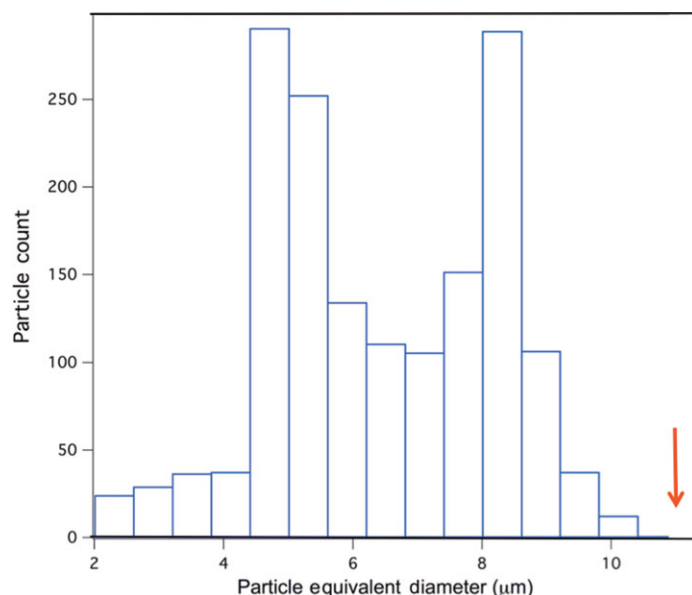


Figure 16. Light obscuration data from 40 μm rods. Red arrow indicates equivalent circular diameter based on dimensions of the rods measured in an SEM averaged over all orientations.

the flow. This tendency was even stronger for the 50 μm rods, while about a third of the less elongated 30 μm rods were noticeably rotated with respect to the flow. Also apparent in the figure are the variation in image sharpness resulting from rods passing through the cell at different depths relative to the focal plane. Figure 18 shows a histogram of the reported ECD measured by Instrument A for the 40 μm rods. The red arrow in the figure corresponds to an ECD calculated from the SEM dimensions. The instrument oversizes particles, yielding a value that is 128% of the SEM ECD value for aligned rods. Oversizing of particles was also observed for Instrument B, especially when run with threshold settings for both dark and light pixels which is the commonly used mode for protein aggregate imaging. From Table 3, it also should be noted the substantial increase in aspect ratio reported by the instruments in comparison with the SEM dimensions. Protein aggregate particles may be more elongated than is often assumed on the basis of FI measurements.

The overestimation of ECD for elongated objects arises from the increasing importance of diffraction effects for these particles. Figure 19 illustrates this point. Figure 19a shows the full field view captured by Instrument A with a rod present just right of center. The inset shows a zoom of the particle, whereas Figure 19b zooms even further so that individual pixels are evident. To define the boundaries of the particle, the software identifies pixels that differ from the background by a threshold amount. The total number of these pixels, combined with the known pixel size, determines the area of the particle. The equivalent diameter of a circle with this area is calculated, and a fixed additional distance is subtracted from this value to produce a reported ECD that produces a good agreement for spherical particles between the measured value and the actual calibrated diameter of the spheres. It is evident, comparing the defined boundary in Figure 19b with the SEM image of a rod produced in the same fabrication (Fig. 19c), that errors related to the diffraction effect extend along the length of the particle.

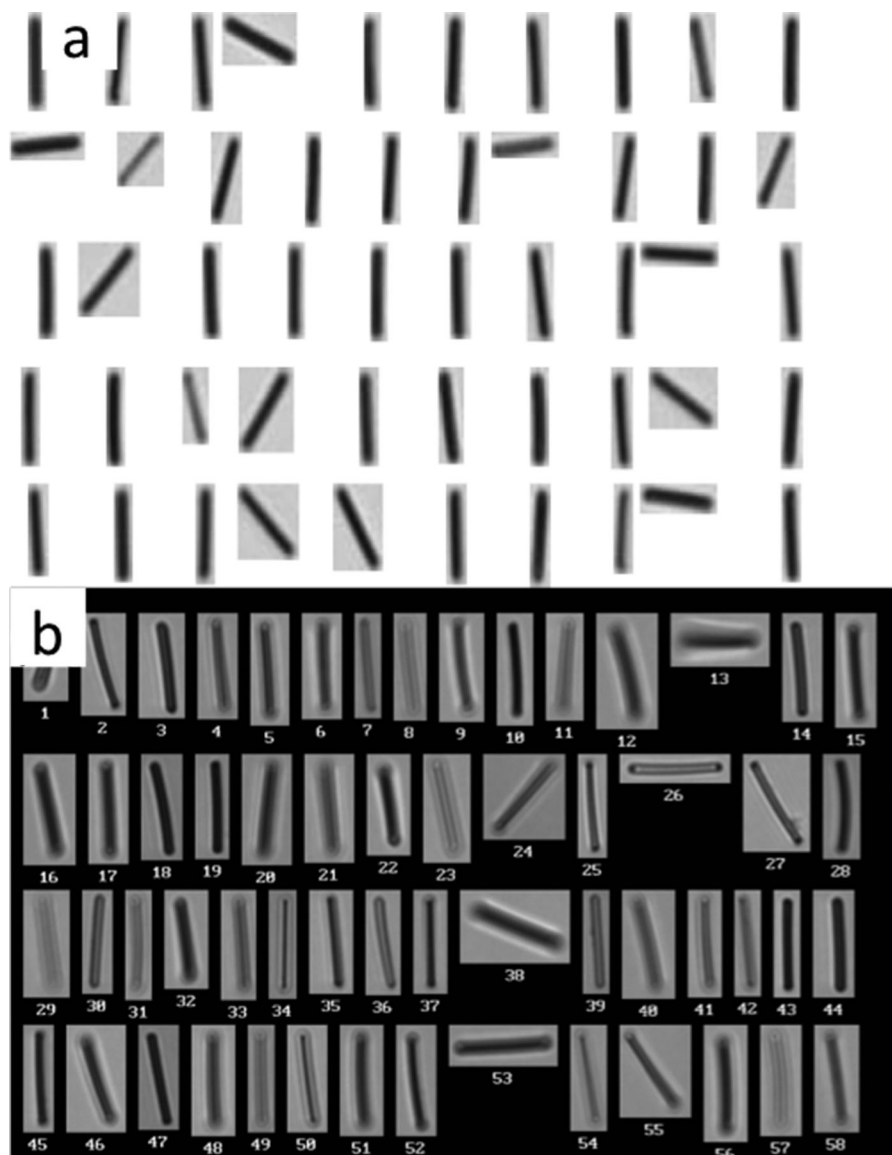


Figure 17. Selection of images of 40 μm rods obtained from (a) Instrument A and (b) Instrument B. Flow direction is vertical.

Thus the error related to diffraction effects comprises a larger fraction of the total area for a rod than for a circular shape.

Rather than subtract a fixed length parameter from the ECD derived from the imaged particle's area A , an alternative scheme would be to subtract a correction area based on the perimeter of the particle and then compute the ECD. An estimate for the areal correction is

$$\delta A = \frac{\delta D}{2} \left(\frac{P_a + P_m}{2} \right) \quad (1)$$

where $\delta D/2$ is the width of the apparent diffraction edge beyond the actual edge of the particle, and P_a and P_m are the actual and measured values of the perimeter. An estimate for P_a is

$$P_a = P_m \left(1 - \frac{\delta D}{D_m} \right) \quad (2)$$

where $D_m = 2(A/\pi)^{1/2}$.

The resulting ECD D_a is then

$$D_a = D_m \left[1 - \frac{\delta D P_m}{4A} \left(2 - \frac{\delta D}{D_m} \right) \right]^{1/2} \quad (3)$$

For a circle this approximation returns the expected $D_a = D_m - \delta D$. The results of comparing the SEM dimensions of the 30, 40, and 50 μm rods, the ECD from Instrument A (with corrections using the subtraction of a fixed δD from the diameter) and the result from using Eq. (3) are presented in Table 4. To obtain the results using Eq. (3), we used measurements of A and P_m from Instrument A. δD was determined from a series of measurements of spheres of different sizes using Instrument A and performing a plot of ECD versus D_m . This yields a straight line. The value of D_m on extrapolating to ECD = 0 is δD , which had the value $\delta D = 6.7 \mu\text{m}$. For the 30 μm rods, imaged rods rotated out of the plane of the image were excluded so that the calculations could be compared to the SEM dimensions. The value of ECD reported by Instrument A differs from the

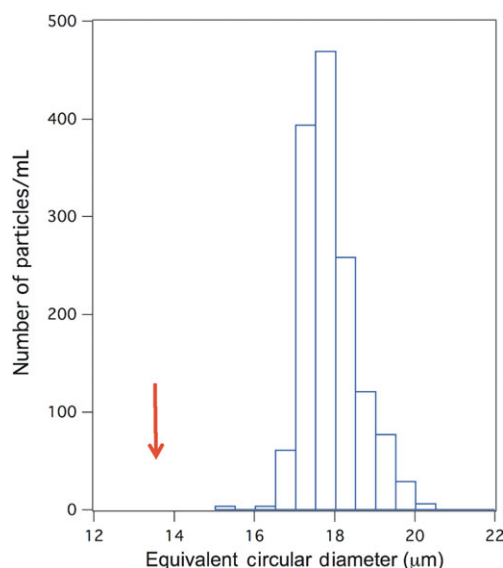


Figure 18. Flow microscopy data from 40 μm rods. Red arrow indicates equivalent circular diameter based on dimensions of the rods measured in a SEM.

Table 4. ECD in Micrometers Based on SEM, FI with Diameter Correction (as Reported Instrument A), and FI with Areal Correction Based on Equation (3), for Rods of Dimensions $31.6 \times 6.6 \times 4.5$, $41 \times 2.8 \times 2.6$, and $51 \times 3.4 \times 2.6 \mu\text{m}^3$

| Method | 30 μm Rod | 40 μm Rod | 50 μm Rod |
|--------------------------|----------------------|----------------------|----------------------|
| SEM | 16.2 | 13.4 | 15.9 |
| FI (diameter correction) | 17.9 | 17.9 | 20.1 |
| FI (areal correction) | 15.4 | 13.1 | 14.6 |

expected value based on SEM dimensions by 10%–34%. Application of the perimeter-based algorithm produces results that differ by only 5% or less for the studied rods.

Defining the correction parameter as δD_{cor} as

$$\delta D_{\text{cor}} = D_m - D_m \left[1 - \frac{\delta DP_m}{4A} \left(2 - \frac{\delta D}{D_m} \right) \right]^{1/2}$$

An example of calculated δD_{cor} for rods with different imaged aspect ratio as a function of ECD is shown in Figure 20. The calculation assumes $\delta D = 6.7 \mu\text{m}$, which as noted above yields $\delta D_{\text{cor}} = 6.7 \mu\text{m}$ for a circle. It is evident that δD_{cor} increases as the shape becomes elongated (lower aspect ratio), accounting for the increased error due to the increased fraction of particle area that is close to an edge.

The selection of thresholding parameters can have a significant effect on size as indicated by the difference in values reported by Instrument B when the threshold is based on dark pixels only versus dark and light pixels. The diffraction of light creates apparent light and dark concentric edges around the perimeters of the particles. For extended rod-shaped particles, with one of the dimensions on the scale of a few microns or less, this can become significant in the calculation of the area-based diameter. Imaging of protein particles is typically performed with thresholding set to both light and dark pixels.

DISCUSSION AND CONCLUSIONS

Particle shape can have a significant influence on the size parameter that different instruments will report. This can also result in particle count differences. If, for example, it is desired to report the number of particles with dimension greater than $2 \mu\text{m}$, if different instruments provide a different size measurement for the same particle, these instruments will effectively have different thresholds for the count totals. It is important to carefully consider the factors that come into the size evaluation that an instrument makes for a particle.

Instruments are generally configured to report an equivalent diameter, which for ESZ is the diameter of a sphere that has the same volume as the measured particle, for LO is the diameter of polystyrene sphere with the same optical cross section as the measured particle, and for FI techniques is the diameter of a circle which has the same area as the photographed particle. When measuring monodisperse polystyrene beads, the four instruments using these different measurement methods agreed within 10% on count and reported size parameter. The only exception was FI Instrument B which oversized the $5 \mu\text{m}$ bead by 21%.

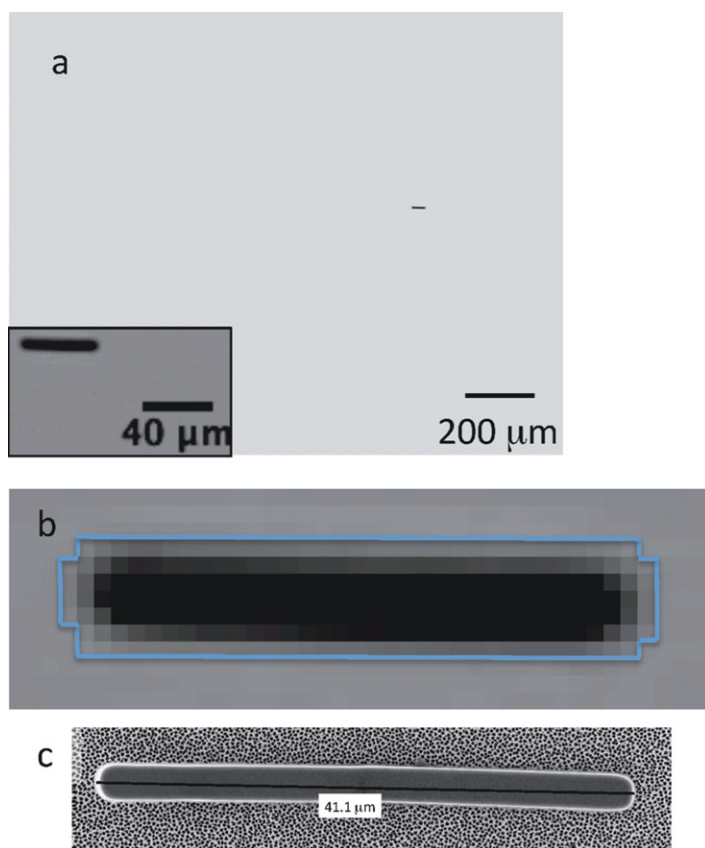


Figure 19. (a) Image showing complete field of view from flow microscopy tool A and inset showing a zoomed-in image of a rod. (b) Further zoomed in image from (a) showing pixilation. Superimposed is an outline corresponding to the pixel area that is assigned to the rod. (c) SEM image of a microfabricated rod of the same dimensions as in (a) and (b) and at the same magnification.

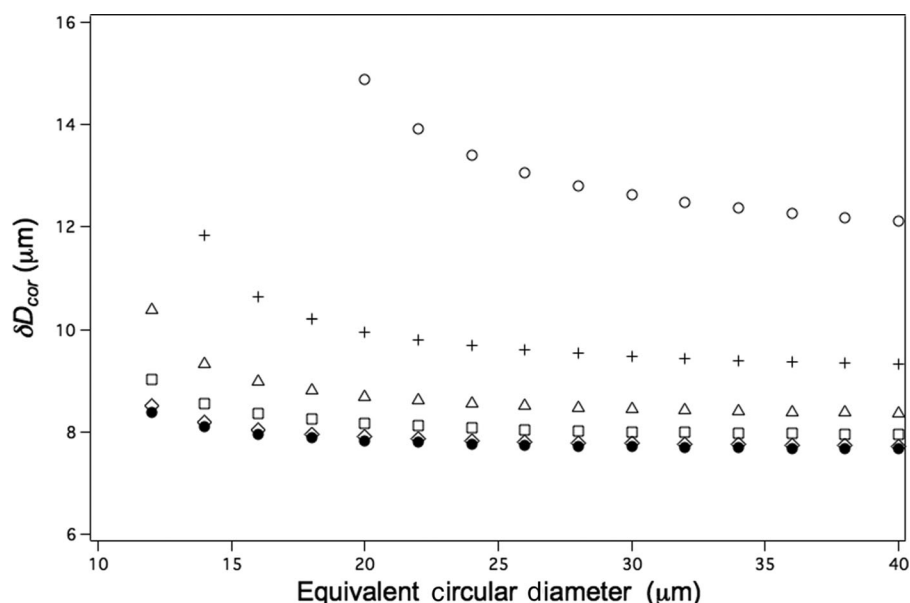


Figure 20. Correction to be subtracted from ECD for rectangle shapes with imaged aspect ratios. Symbols represent the aspect ratios used to generate data points according to: circle 0.15, plus 0.3, triangle 0.45, square 0.6, diamond 0.8, and filled circle 1.

Using microfabricated, monodisperse rods as test particles revealed significant differences in the reported size parameters. Elongated rods, corresponding to fibers, tend to align with the flow. In the ESZ instrument, this produced a reduction in signal compared to an equivalent size sphere, as the particle cuts across fewer electric field lines. COMSOL calculations confirm the effect. For the 40 μm rod, this constituted a 30% reduction in signal compared with a sphere, and because signal is proportional to the cube of the diameter, a 12% reduction in reported ESD. Tumbling of the particles acts in the opposite direction, producing signals as large as or larger than the signal that would be produced by an equivalent sphere. The propensity to tumble is sensitive to the aspect ratio of the particle, with elongated particles less likely to tumble. Propensity to tumble was insensitive to flow rate, as the flow rates used and dimensions of the device produce laminar flow. Tumbling is induced by shear forces present when elongated objects interact with the flow field established by the microchannel geometry at the constriction.

For the fabricated rods used in this study, FI measurements gave a measured ECD that exceeded the volumetric ESD predicted from the known rod geometry by a factor of ≈ 2 . It was observed that rods tend to align with the flow. This results in an equivalent diameter measurement that is larger than the equivalent diameter of a sphere with the same particle volume. Thus, for a given elongated particle that aligns in the flow, FI instruments will report a larger diameter than volume-measuring instruments. Compounding this effect is the diffraction effect associated with the boundary of small elongated particles. Unless an instrument is operated in a mode that minimizes diffraction errors, the added width produced by the interference will produce a larger error in the area than is normally corrected for with spherical particles. A new algorithm correction based on the use of the measured perimeter of a particle reduced this effect. Diffraction and focus effects also cause the reported aspect ratio to be as much as double the actual aspect ratio of rods, suggesting that actual protein aggregates

imaged by these instruments may have an aspect ratio that is smaller than reported by the instrument.

For LO, the range of diameters reported agreed reasonably well with expectations for tumbling particles. However, the average particle diameter was approximately 30%–50% smaller than expected from a geometrical analysis of either aligned or randomly tumbling particles. Study of the geometry of the particle illumination and detection of scattered light provides plausible reasons for this undersizing, but a detailed explanation is hampered by the lack of knowledge of the exact optical arrangement inside the sensor heads.

Further study is needed to better understand the effects observed here and their relationship to measurements on protein aggregates. For the LO results, comparison of response for instruments with different thicknesses of the illumination zone and capture of the full scattering signal may help to understand why the instrument reports diameters smaller than expected. It would be desirable to learn how irregular particles (such as protein aggregates) tumble. For the case of ESZ, instrumental analysis of signal shape may be used to deduce if an event represents a particle which has tumbled. In addition to shape effects, particle porosity may be important for protein particles. If the electrolyte penetrates interconnected pores, there will be a decrease the electrical signal of a particle compared to a nonporous particle of similar external dimension. Future work using the microfluidic ESZ/FI will examine this possibility. Ultimately the differences in size distribution produced by orthogonal methods may be useful indicators of particle properties that are in addition to size and count.

ACKNOWLEDGMENTS

Fabrication of the SU-8 rods and microfluidic structures was carried out at the NIST Center for Nanoscale Science and Technology (CNST). We thank Dan Berdovich of Micro

Measurement Laboratories for helpful suggestions and insights on LO counters.

REFERENCES

1. Rosenberg AS. 2006. Effects of protein aggregates: An immunologic perspective. *AAPS J* 8(3):E501–E507.
2. Demeule B, Messick S, Shire SJ, Liu J. 2010. Characterization of particles in protein solutions: Reaching the limits of current technologies. *AAPS J* 12(4):708–715.
3. Barnard JG, Rhyner MN, Carpenter JF. 2012. Critical evaluation and guidance for using the coulter method for counting subvisible particles in protein solutions. *J Pharm Sci* 101(1):140–153.
4. Werk T, Volkin DB, Mahler HC. 2014. Effect of solution properties on the counting and sizing of subvisible particle standards as measured by light obscuration and digital imaging methods. *Eur J Pharm Sci* 53:95–108.
5. Zolls S, Gregoritz M, Tantipolphan R, Wiggenhorn M, Winter G, Friess W, Hawe A. 2013. How subvisible particles become invisible—relevance of the refractive index for protein particle analysis. *J Pharm Sci* 102(5):1434–1446.
6. Jennings BR, Parslow K. 1988. Particle-size measurement—The equivalent spherical diameter. *Proc R Soc Lond A Mat* 419(1856):137–149.
7. Sharma DK, King D, Oma P, Merchant C. 2010. Micro-flow imaging: Flow microscopy applied to sub-visible particulate analysis in protein formulations. *AAPS J* 12(3):455–464.
8. Joubert MK, Luo QZ, Nashed-Samuel Y, Wypych J, Narhi LO. 2011. Classification and characterization of therapeutic antibody aggregates. *J Biol Chem* 286(28):25118–25133.
9. Lloyd P. Response of the electrical sensing zone method to non-spherical particles Particle Size Analysis, Loughborough, England John Wiley & Sons, 1981, pp 199–208.
10. Kachel V. 1979. Electrical resistance pulse sizing (Coulter sizing). In *Flow cytometry and sorting*; Melamed MR, Mullaney PF, Mendelsohn ML, Eds. New York: John Wiley & Sons, Inc., pp 61–104.
11. Ferreira PJ, Rasteiro MG, Figueiredo MM. 1993. Influence of shape on particle size analysis. *Part Sci Technol* 11:199–206.
12. Shekunov BY, Chattopadhyay P, Tong HHY, Chow AHL. 2007. Particle size analysis in pharmaceuticals: Principles, methods and applications. *Pharm Res Dordr* 24(2):203–227.
13. Certain commercial instruments are identified to adequately specify the experimental procedure. In no case does such identification imply endorsement by the National Institute of Standards and Technology.
14. Tao SL, Popat KC, Norman JJ, Desai TA. 2008. Surface modification of SU-8 for enhanced biofunctionality and nonfouling properties. *Langmuir* 24(6):2631–2636.
15. Wilson GA, Manning MC. 2013. Flow imaging: Moving toward best practices for subvisible particle quantitation in protein products. *J Pharm Sci* 102(3):1133–1134.
16. Berge LI, Jossang T, Feder J. 1990. Off-axis response for particles passing through long apertures in coulter-type counters. *Meas Sci Technol* 1(6):471–474.
17. Einarsson J, Johansson A, Mahato SK, Mishra YN, Angilella JR, Hanstorp D, Mehlig B. 2013. Periodic and aperiodic tumbling of microrods advected in a microchannel flow. *Acta Mech* 224(10):2281–2289.
18. Knollenberg RG, Gallant RC. February, 1990. International Conference on Particle Detection, Metrology and Control, pp Arlington, Va USA 154–182.
19. Bohren CF, Huffman DR. 1998. Absorption and scattering of light by small particles: Wiley Science. Weinheim, Germany
20. Chen TW. 1995. Effective sphere for spheroid in light-scattering. *Opt Commun* 114(3–4):199–202.
21. vande Hulst HC. 1957. Light scattering: By small particles. New York: John Wiley & Sons.